

Exploring Real&Synthetic Dataset and Linear Attention in Image Restoration

Yuzhen Du^{1*} Teng Hu^{1*} Jiangning Zhang^{2,3} Ran Yi^{1†} Chengming Xu²
Xiaobin Hu² Kai Wu² Donghao Luo² Yabiao Wang² Lizhuang Ma¹

¹Shanghai Jiao Tong University ²Youtu Lab, Tencent ³Zhejiang University

Code: <https://github.com/YuzhenD/Resyn>

Abstract

*Image restoration (IR) aims to recover high-quality images from degraded inputs. Recent advancements in deep learning have significantly improved image restoration performance. However, existing methods lack a unified training benchmark specifying training iterations and configurations. Additionally, we construct an image complexity evaluation metric using the gray-level co-occurrence matrix (GLCM) and find a bias between the image complexity distributions of commonly used IR training and testing datasets, leading to suboptimal restoration results. Therefore, we construct a new large-scale IR dataset called ReSyn, that utilizes a novel image filtering method based on image complexity to achieve a balanced image complexity distribution and contains both real and AIGC synthetic images. From the perspective of measuring the model’s convergence ability and restoration capability, we construct a unified training standard that specifies the training iterations and configurations for image restoration models. Furthermore, we explore how to enhance the performance of transformer-based image restoration models based on linear attention mechanisms. We propose **RWKV-IR**, a novel image restoration model that incorporates the linear complexity RWKV into the transformer-based image restoration structure, and enables both global and local receptive fields. Instead of directly integrating Vision-RWKV into the transformer architecture, we replace the original Q-Shift in RWKV with a novel Depth-wise Convolution shift to effectively model the local dependencies. It is further combined with Bi-directional attention to achieve both global and local aware linear attention. Moreover, we propose a Cross-Bi-WKV module that combines two Bi-WKV modules with different scanning orders to achieve balanced attention for horizontal and vertical directions. Extensive quantitative and qualitative experiments demonstrate the effectiveness of our RWKV-IR model. Project: <https://yuzhend.github.io/ReSyn.github.io/>*

1. Introduction

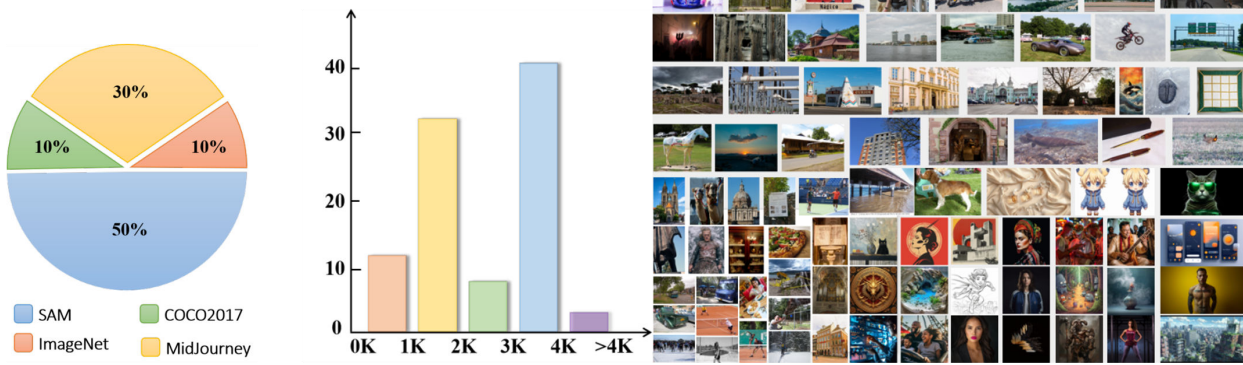
Image restoration (IR), which aims to recover high-quality images from low-quality degraded inputs, is a crucial task in modern image processing. This field encompasses various sub-tasks, including super-resolution, image denoising, and compression artifacts reduction. Recently, the advancements of deep learning techniques, such as Convolutional Neural Networks (CNNs) [11, 13, 33, 57, 63] and Transformers [6, 7, 10, 30, 32], have significantly enhanced image restoration performance, driving continuous progress in this field. Reviewing the previous IR methods, more complex and deeper models [7, 67] often achieve better performance.

To meet the data requirements for IR model training, a large number of images need to be collected to construct a paired training dataset. Due to limited photography and compression techniques, the images in the previous training datasets often have the problem of blurring or noise, meanwhile, the images in some test datasets have more image details, this causes the domain gap (different image complexities) between the commonly used training and test datasets [31]. Most datasets [31, 44] focused on collecting a large number of images of high resolution, few consider how to measure and address this domain gap.

In this paper, we construct an image complexity metric based on the Gray-Level Co-occurrence Matrix (GLCM) analysis method, and reveal a significant bias in image complexity distribution within classic IR training datasets and test datasets. We further utilize this metric as a criterion for filtering the image restoration dataset and construct a new image restoration dataset, which is called **ReSyn dataset**. In many previous datasets [31, 44], resolution and Bits Per Pixel (BPP) have been used as important criteria for image filtering, but they are insufficient for constructing *image complexity balanced datasets*. To this end, we further utilize the GLCM-based image complexity metric we proposed to filter and retain some images of medium resolution but with high image complexity. Moreover, with the rapid development of AI-generated content (AIGC), there is a surging demand for synthetic image restoration. We consider the generated images as an essential part of the dataset and filter them in

*Equal contribution. Jiangning Zhang leads this project.

†Corresponding author.



a) The proportion of ReSyn dataset b) The resolution distribution of ReSyn c) Some images from ReSyn dataset.

Figure 1. The diversity analysis of our ReSyn dataset. It contains both real and synthetic images from a variety of data sources and covers a wide range of resolutions.

the same manner, which also enriches the sources of our dataset. The final ReSyn dataset comprises 12,000 images, with 30% being high-quality synthetic images sourced from the web. Our ReSyn dataset also presents a wide range of image resolutions, ranging from 0.25K to 4K, and originates from various sources.

We also review the training processes of previous image restoration models and find that there is a lack of a **unified IR training benchmark**, *i.e.*, the training iterations and configurations are not unified. Considering the model’s convergence and restoration capability, we construct a set of training standards. To measure the model’s convergence capability, we use a shorter number of training iterations; to measure the restoration capability, we use a longer number of training iterations. This combination of short and long training iterations allows users to have a more comprehensive understanding of the model’s capabilities, facilitating the selection of the model. We conduct a comprehensive evaluation of SOTA IR models using the unified training standard, on our ReSyn dataset and other commonly used IR datasets. Both the ReSyn dataset and the constructed unified training standard form our proposed benchmark.

When comparing various image restoration models, we notice that the linear attention mechanism (*e.g.*, Mamba-based IR models) has great potential for enhancing the effective receptive field of models. Therefore, we aim to incorporate a linear complexity attention mechanism, RWKV [41], with the image restoration models. Based on the commonly used transformer-based IR structure, we construct our **RWKV-IR**, which consists of three stages: shallow feature extraction, deep-feature enhancing, and HQ image reconstruction modules. We mainly incorporate RWKV into the second stage, deep-feature enhancing. We first introduce the Vision RWKV module to extract the deep image features, where a Spatial Mix Layer is employed to enable

our model with global receptive fields with only linear computational complexity. Then, to enhance the modeling of relationships in local receptive fields and eliminate the negative effects caused by the original Q-shift operation, we exploit the characteristics of the local receptive fields in convolutional operations, and propose a **Depth-wise Convolution Shift (DC-shift)** module, as a replacement of the original Q-shift of the RWKV module. Moreover, the Bi-WKV method of original Vision-RWKV has an unbalanced position embedding, paying more attention to the horizontal direction and less attention to the vertical direction, which is not suitable for the IR tasks. We propose a **Cross-Bi-WKV module**, which combines two Bi-WKV modules with different scanning orders to achieve a balanced attention to surrounding features. By cross-scanning and synchronizing the calculations of the two Bi-WKV modules in both horizontal and vertical directions, we achieve a balanced attention to all four directions. Extensive quantitative and qualitative experiments demonstrate the effectiveness of our RWKV-IR. We summarize our contributions as below:

- We propose a comprehensive benchmark for image restoration tasks, which includes a novel large-scale benchmark dataset, and a unified training standard that specifies the number of training iterations and the configuration of batch size. We conduct a comprehensive evaluation of SOTA IR models using the unified training standard on the new dataset and other common IR datasets.
- We construct a large-scale dataset called ReSyn, that integrates both real and synthetic images. This dataset encompasses a variety of data sources and utilizes novel image filter methods based on our newly proposed GLCM-based image complexity metric.
- We design RWKV-IR, a novel image restoration model with both global and local receptive fields, which can effectively restore low-quality images with linear compu-

tational complexity. We replace the original token-shift method (Q-shift) with Depth-wise Convolution shift for local dependencies modeling, and proposes Cross-Bi-WKV to replace Bi-WKV for more balanced attention for horizontal and vertical directions, which enables RWKV to be effectively transferred to IR models.

2. Related Works

2.1. Image Restoration

Image restoration has witnessed significant progress with the advent of computer vision [8, 21, 32, 54], exemplified by pioneering CNN-based methods like SRCNN [13], DnCNN [57], and ARCNN [14], targeting super-resolution, denoising, and artifact reduction [5, 11, 18, 25, 27, 47, 48, 61, 64, 65]. Despite their success, CNN-based approaches often struggle to model global dependencies effectively. Meanwhile, Transformers, proven competitors to CNNs in various computer vision tasks [4, 15, 36, 53, 55], show promise in restoration tasks. However, they encounter challenges due to the quadratic computational complexity of the attention mechanism [45]. Strategies like IPT [6] and SwinIR [32] address this by employing patch-based processing and shifted window attention. But the trade-off persists between efficient computation and global modeling [7, 9, 10, 29, 50, 56]. Recently, MambaIR [21] has been proposed to incorporate Mamba [19, 35] into the image restoration task, which globally processes the image features with only linear computational complexity. Following this trend, this paper explores the possibility of integrating another linear attention mechanism, RWKV (which has shown better performance in other vision tasks [17, 20, 22]), into image restoration models.

Single Image Restoration Datasets. Learning-based image restoration methods rely on the external training dataset to learn the mapping between degraded and GT images. But most training datasets [31, 44] focus on collecting higher resolutions and larger quantities of real images, few considering the bias between the training and testing datasets, and there is no dataset taking the synthetic images into account. In this paper, we construct an image complexity metric based on GLCM analysis and find that the commonly used training datasets [33, 44] for SR task and [2, 37] for image denoising task, exhibit a certain distribution difference in resolution compared to the testing datasets [3, 23, 38, 39, 51]. Therefore, we utilize this metric as a filter criterion and construct a new image ReStoration dataset which including the Real and Synthetic images.

2.2. Receptance Weighted Key Value (RWKV)

The attention mechanism has shown promising performance in both CV and NLP fields. Various operators with linear complexity [19, 41, 43] have been explored to optimize the

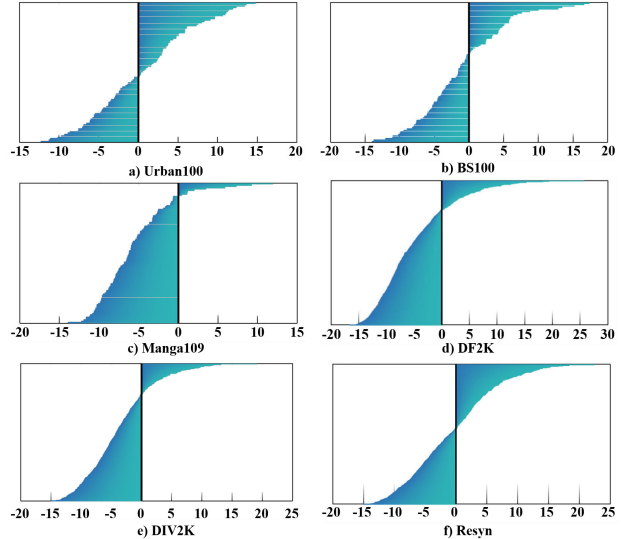


Figure 2. The complexity distributions of different datasets. The complexity distributions of the training datasets DIV2K [44] and DF2K [33] have a typical shift, containing more images of low complexity. Our ReSyn dataset balances the distribution of low and high complexity images by image filtering based on the newly proposed GLCM image complexity measure.

global attention mechanism in recent years. A modified form of linear attention, the Attention Free Transformer (AFT) [52], paved the way for the RWKV architecture by using some attention heads equal to the size of the feature dimension and incorporating a set of learned pairwise positional biases. RWKV-v4 [41] employed exponential decay to model global information efficiently. Vision-RWKV [16] transfers the RWKV-v4 to the vision domain through a Q-shift mechanism and bidirectional attention. RWKV-5/6 [42] further refined the architecture of RWKV-4. RWKV-5 adds matrix-valued attention states, LayerNorm over the attention heads, SiLU attention gating, and improved initialization. It also removes the Sigmoid activation of receptance. RWKV-6 further applies data dependence to the decay schedule and token shift. We modify the RWKV-v4 module of Vision-RWKV, use a depth-wised conv to replace the Q-shift, and also a Cross-Bi-Direction attention to replace the Bi-Direction attention.

3. ReSyn Dataset

Due to ndlimited photography techniques and compression techniques, many images in previous datasets [12, 44] suffer from noise, blurring, and other problems. However, most datasets focus solely on obtaining high-resolution images, using resolution and Bits Per Pixel (BPP) for image filtering, but lacking sufficient consideration for image complexities. This causes a distribution bias (different image complexities)

between the classic image restoration training datasets and the test datasets. We propose an image complexity metric based on the Gray Level Co-occurrence Matrix (GLCM) analysis method to directly analyze this complexity distribution bias. As shown in Fig. 2, we analyze the GLCM complexity distribution of the classic SR training datasets (DIV2K [44] and DF2K [33]), and test datasets (Urban100, Manga109 and BS100). It can be seen that the classic SR training datasets and test datasets often have different image complexity distributions. And the test dataset that often achieves a better PSNR performance, *e.g.*, Manga109, has a complexity distribution closer to that of the training dataset. We further analyze the relationship between the GLCM complexity indicator and the restoration performance metric PSNR. As shown in Fig. 3, GLCM complexity can better predict the restoration performance compared to the BPP indicator. Moreover, datasets with lower complexity show better restoration performance.

To enhance the performance of existing methods and incorporate images generated by the AIGC method, we construct the ReSyn dataset, a new large-scale dataset for both the Real and Synthetic image ReStoration. Our dataset introduces the GLCM complexity indicator as a criterion for filtering images to help improve the quality of shuffled images and achieve a balanced complexity distribution. Examples of the images from our ReSyn dataset are shown in Fig. 1. The data collection pipeline and the dataset analysis are introduced in details below.

3.1. DATA COLLECTION

Data Source. Our dataset consists of real and AI-generated images. Previous methods [7, 67] improve performance by pretraining on large-scale datasets like ImageNet [12]. We follow this trend and borrow images from these datasets to form the real image part of our dataset. The real images are collected from the commonly used large-scale datasets for high-level tasks, including ImageNet [12], COCO2017 [34], and SAM [26]. The images are shuffled and low-quality images are discarded, only 9K images are retained. To introduce the AI-generated images into this dataset, we automatically crawl images from Midjourney, and after filtering we retain 3K synthetic images for our dataset. The origins of these image distribution charts and the diversity of their resolutions are illustrated in Fig. 1. Different from previous datasets that filter solely based on resolutions, we do not completely discard images with resolutions below 2K, since many images in the test dataset are below 2K resolution and have a high image complexity. Our dataset encompasses a broad range of image resolutions from 0.5K to 4K, and most images have a resolution larger than 1K.

Data Selection Criteria. The images used for image restoration model training need to have a high pixel-level quality. To this end, we divide the shuffle process into three steps. 1)

Firstly, the images of resolution smaller than 800×800 are discarded, since for super-resolution tasks, the images need to be down-sampled. This can help remove most low-quality images. 2) Secondly, to remove the blurry or noisy degraded images, we follow the blur and noise suppression process proposed in LSDIR [31]. The remaining images are under blur detection by the variance of the image Laplacian, and flat region detection through the Sobel filter. 3) Thirdly, all the images are shuffled through the GLCM complexity metric (detailed below) to ensure a balanced distribution. We ensure that the number of images with complexity values below zero is equal to that above zero. Therefore, we can form a dataset of balanced image complexity distribution. It should be mentioned that images from different sources are filtered individually.

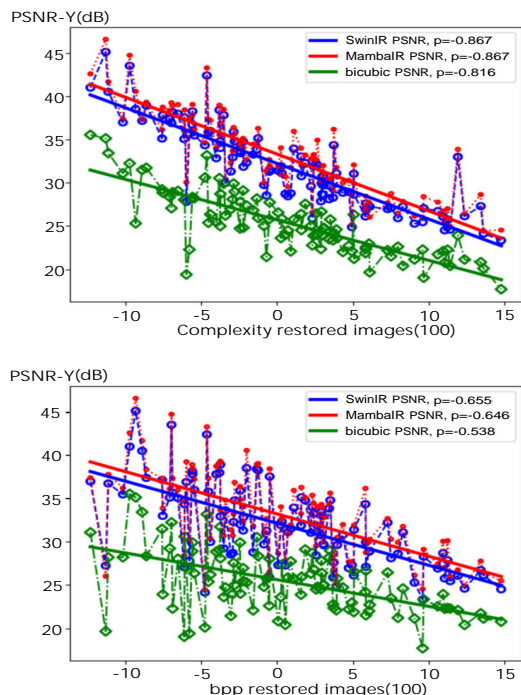


Figure 3. PSNR ($\times 2$ SR on Urban100 [23]) performance can be predicted by the proposed GLCM image complexity and BPP [44]. We conduct this analysis on MambaIR, SwinIR, and bicubic up-sampling restored images.

Image Complexity Analysis. As shown in previous works [44], the PSNR metric of super-resolution images is strongly correlated with the Bits Per Pixel (BPP), an indicator for the quantity of image information. Although BPP reflects the quality of an image by measuring its color depth, it lacks consideration for the relationships between pixels and cannot adequately measure the texture variation and complexity of an image. Therefore, this paper further measures the image complexity based on the Gray Level Co-occurrence Matrix (GLCM) and investigates its correlation

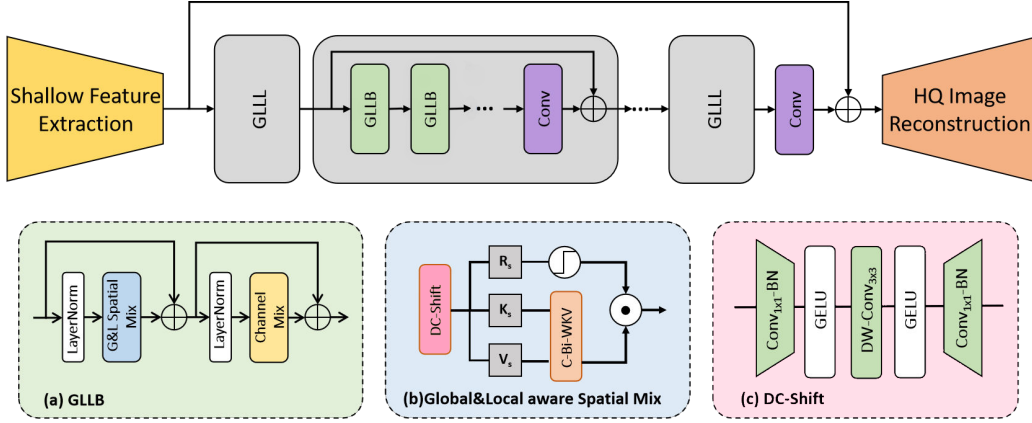


Figure 4. **Framework of our RWKV-IR**, which consists of three stages: shallow feature extraction, deep feature enhancing, and HQ image reconstruction. For deep feature enhancing, a series of Global&Local Linear attention Layers (GLLL, which is based on RWKV) and a Conv Block are used. Each GLLL contains several GLLB blocks.

with PSNR metric. Since human eyes are more sensitive to texture, we utilize the GLCM, which is closely related to the complexity of image texture, to construct an image complexity analysis metric. We calculate relevant statistical quantities from the GLCM, and use Entropy, Energy, and Dissimilarity to build a formula for image complexity analysis as follows: $I_{complexity} = ENT - ENE + DISS$, where ENT , ENE , and $DISS$ represent entropy, energy, and dissimilarity respectively, all of which are statistical quantities calculated from GLCM. As shown in Fig. 3, we analyze the correlation between the PSNR-Y metric and GLCM-based image complexity, as well as BPP. The PSNR metrics are measured on super-resolution results generated by two pre-trained models and a direct bicubic upsample for the Urban100 test images, and sorted according to GLCM complexity and BPP. Our GLCM complexity measure has a stronger Pearson correlation ($\rho = -0.86$) compared to BPP ($\rho = 0.65$), indicating that the proposed image complexity is a stronger predictor for the PSNR metric of the restored images. Furthermore, the distribution of GLCM complexity is symmetric with respect to the origin, making it an excellent metric for image filtering. **Post Processing.** For the classic image restoration tasks, *e.g.*, super-resolution, the training requires paired down-sampled LR images and GT. We employ the classic bicubic down-sampling method¹ to obtain the LR images. We use the commonly used scale factors of $\times 2$, $\times 3$, and $\times 4$.

Partitions. After the shuffle and the post-processing, there are 12K images left, of which 9K are real images and 3K are synthetic images. We then randomly partition our ReSyn dataset into a training set of 10K images, a validation set of 1K images, and a test set of 1K images.

¹Simulating MATLAB’s anti-aliasing imresize using a Python-based approach, with negligible differences in visual effects.

4. Methodology: RWKV-IR

The Receptance Weighted Key-Value model (RWKV) [41] is a linear complexity attention mechanism that combines the advantages of RNN and Transformer. Its linear complexity enables the utilization of a broader range of pixels for activation, which is suitable for image restoration tasks. Consequently, we integrate this linear complexity attention mechanism with a classic image restoration model to construct our **RWKV-IR**. The framework of our RWKV-IR is illustrated in Fig. 4, following the widely used structure [21, 32] that consists of three stages: shallow feature extraction, deep feature enhancing, and high-quality image reconstruction, where the RWKV is mainly incorporated into the second stage. 1) Shallow feature extraction: Given a low-quality input $I_{LQ} \in \mathbb{R}^{H \times W \times 3}$, a 3×3 convolution layer first extracts the shallow feature $F_S \in \mathbb{R}^{H \times W \times C}$, where H and W represent the height and width, and C is the number of channels in the shallow feature. 2) Deep feature enhancing: Subsequently, a series of Global&Local Linear attention Layers (GLLL, which is based on RWKV) and a 3×3 Convolution Block perform deep feature extraction. Each GLLL layer contains several GLLB blocks. Afterwards, a global residual connection fuses the shallow feature F_S and the deep feature F_D into a hybrid feature $F_H = F_S + F_D$, which is then input into the high-quality image reconstruction module. 3) High-quality image reconstruction: Finally, the high-quality reconstruction module outputs a restored image $I_{RE} \in \mathbb{R}^{(H \times s) \times (W \times s) \times 3}$, where s is the scale factor used for the super-resolution task.

Global&Local Linear attention Block (GLLB). Transformer-based restoration networks [7, 32] typically design the core block for restoration following a $norm \rightarrow Attention \rightarrow norm \rightarrow MLP$ workflow. The *Attention* module is designed to model global dependency,

but due to heavy computational complexity, only local window attention is used. Therefore, replacing the local attention with a linear complexity attention mechanism can reduce the computational overhead while increasing the window size, to better model global dependencies. Therefore, we aim to introduce the Receptance Weighted Key Value (RWKV) module to enhance the image restoration effects. However, simply replacing the *Attention* module with the Spatial Mix from RWKV, and replacing the *MLP* module with the Channel Mix from RWKV yields sub-optimal results (as shown in Tab. 4, 5). We find that the linear complexity attention module from RWKV can model global dependencies well, but its utilization of local information is insufficient. Through further experiments, we find that this is caused by the Q-shift and the Bi-direction WKV in the original RWKV, which are transferred from the NLP tasks and not suitable for the low-level vision tasks. Therefore, we replace the Q-shift with a newly proposed **Depth-wise Convolution shift (DC-shift)** to achieve better visual representation and easier optimization [7, 49, 66]. Moreover, we propose a **Cross-Bi-WKV module** that integrates two Bi-WKV modules with different scanning orders, instead of the original Bi-WKV, to balance the attention for horizontal and vertical directions and improve the model performance.

As shown in Fig. 4(a), we propose a **Global&Local Linear attention Block (GLLB)**, which follows a $norm \rightarrow Conv \rightarrow Attention \rightarrow norm \rightarrow Channel-Mix$ workflow, with two residual connections. Given an intermediate feature F_i , where i represents the i -th GLLB block. A LayerNorm module is followed by a linear complexity

Global&Local-Aware Spatial Mix module, that models both long-term dependencies and local dependencies: $F_{g,i} = GLSpatial-Mix(LN(F_i))$. The local-aware characteristics are achieved by replacing the Q-Shift in the original Spatial Mix with our Depth-wise Convolution shift (DC-Shift, detailed below). Furthermore, the Channel Mix module replacing the *MLP* is used for stabilizing the training process and avoiding channel oblivion: $F_{i+1} = F_{g,i} * \beta + LN(Channel-Mix(F_{g,i}))$.

DC-Shift. To emulate the memory mechanism of RNNs, the original RWKV proposes a token shift mechanism. Consider an input feature $X \in \mathbb{R}^{T \times C}$ (where $T = H \times W$), it is first shifted, and then fed into three linear layers to obtain the ma-

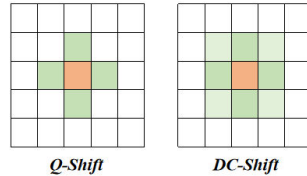


Figure 5. Different shift methods. The Q-shift is a simple channel replacement operation using four neighboring pixels, while our DC-shift is a depth-wise conv leveraging the surrounding pixels in a $k \times k$ neighborhood.

trices $R_s, K_s, V_s \in \mathbb{R}^{T \times C}$: $R_s = Shift_R(X)W_R, K_s = Shift_K(X)W_K, V_s = Shift_V(X)W_V$. Then, K_s and V_s are used to calculate the global attention $wkv \in \mathbb{R}^{T \times C}$ by a linear complexity bidirectional attention mechanism, and multiplied with $\sigma(R_s)$ which controls the output O_s probability. But the original implementation of *Shift* is a Q-shift operation, which simply combines the features from the top, left, down, and right neighboring pixels, each using $C/4$ channels, to replace the feature of the center pixel, formulated as follows:

$$Q-Shift_{(*)}(X) = X + (1 + \mu_{(*)})X', \text{ where } X'[h, w] = \text{Concat}(X[h-1, w, 0 : C/4], X[h+1, w, C/4 : C/2], X[h, w-1, C/2 : 3C/4], X[h, w+1, 3C/4 : C]). \quad (1)$$

The Q-Shift is not suitable for image restoration due to two reasons: 1) In image restoration tasks, the number of channels in the features is relatively small compared to NLP tasks; and 2) The simple feature substitution in Q-Shift does not consider the similarity between local pixels, making it not suitable for image restoration tasks that rely on local similarity. Therefore, we propose a **Depth-wise Convolution Shift (DC-Shift)** shown in Fig. 5 to replace the Q-shift, which helps enhance the model performance by modeling the relationships in local receptive fields. As shown in Fig. 4(c), the Depth-wise Convolution shift consists of two 1×1 Convolution Layers and one $k \times k$ Depth-wise Convolution Layer. By using this structure, we can reduce the number of parameters compared to using the classic channel convolution module and also compensate for the lack of local features. The calculation process of this DC-Shift module is formulated as: $F_{l,i} = Conv_{1 \times 1}(GeLU(DW-Conv_{k \times k}(GeLU(Conv_{1 \times 1}(X)))))$, where k is the kernel size of the depth-wise convolution. By combining the Depth-wise Convolution Shift with Bi-directional attention, as shown in Fig. 4(b), we achieve Global&Local-Aware Spatial Mix.

Cross-Bi-WKV module. The core idea of the Vision-RWKV is the linear complexity Bi-directional attention (Bi-WKV). Its calculation result for the t -th pixel is below:

$$wkv_t = Bi-WKV(K, V)_t = \frac{\sum_{i=0, i \neq t}^{T-1} e^{-(|t-i|-1)/T} \dot{w} + k_i v_i + e^{u+k_t} v_t}{\sum_{i=0, i \neq t}^{T-1} e^{-(|t-i|-1)/T} \dot{w} + k_i v_i + e^{u+k_t}}, \quad (2)$$

where the upper limit for the current pixel t (the $t - th$ pixel after flattening the 2D pixels into a 1D sequence using the horizontal scanning order) is set to $T - 1$ (the last pixel), to ensure that all pixels are mutually visible in the calculation of each other's result. In this formula, $(|t - i| - 1)/T$ is used as the position embedding, which is unbalanced for horizontal and vertical directions, *i.e.*, the position embedding differences between the left and right neighboring

Table 1. Quantitative comparison on **classic image super-resolution** with state-of-the-art methods on 10K iters training. The best and the second best results are in red and blue.

Method	scale	dataset	Set5		Set14		BSDS100		Urban100		Manga109		ReSyn	
			PSNR	SSIM	PSNR	SSIM	PSNR	SSIM	PSNR	SSIM	PSNR	SSIM	PSNR	SSIM
HAN [40]	×2	DF2K	38.26	0.9611	34.01	0.9205	32.36	0.9008	33.09	0.9366	39.56	0.9788	35.22	0.9311
SwinIR [32]	×2	DF2K	38.25	0.9616	34.04	0.9215	32.39	0.9024	33.06	0.9365	39.54	0.9790	35.24	0.9313
SRFormer [67]	×2	DF2K	34.80	0.9301	30.74	0.8495	29.33	0.8113	29.12	0.8712	34.68	0.9510	32.30	0.8763
MambaIR [21]	×2	DF2K	38.34	0.9617	34.42	0.9246	32.45	0.9032	33.55	0.9401	39.78	0.9796	35.40	0.9325
RWKV-IR (Ours)	×2	DF2K	38.38	0.9618	34.42	0.9246	32.46	0.9034	33.59	0.9404	39.80	0.9797	35.44	0.9327
HAN [40]	×2	ReSyn	38.08	0.9002	33.88	0.9198	32.30	0.9011	33.10	0.9352	39.15	0.9733	35.46	0.9328
SwinIR [32]	×2	ReSyn	38.18	0.9616	34.03	0.9213	32.39	0.9026	33.12	0.9370	39.30	0.9791	35.52	0.9331
SRFormer [67]	×2	ReSyn	38.17	0.9621	34.12	0.9224	32.41	0.9031	33.39	0.9396	39.50	0.9797	35.62	0.9340
MambaIR [21]	×2	ReSyn	38.26	0.9616	34.43	0.9247	32.46	0.9034	33.54	0.9401	39.72	0.9794	35.64	0.9350
RWKV-IR (Ours)	×2	ReSyn	38.28	0.9618	34.42	0.9245	32.47	0.9032	33.58	0.9404	39.76	0.9796	35.68	0.9352
HAN [40]	×3	DF2K	34.77	0.9300	30.60	0.8466	29.28	0.8110	29.03	0.8701	32.56	0.9451	32.25	0.8744
SwinIR [32]	×3	DF2K	34.80	0.9301	30.74	0.8495	29.33	0.8113	29.12	0.8712	34.65	0.9501	32.30	0.8763
SRformer [67]	×3	DF2K	34.62	0.9306	30.73	0.8501	29.39	0.8132	29.53	0.8784	34.92	0.9524	32.38	0.8779
MambaIR [21]	×3	DF2K	34.86	0.9307	30.76	0.8505	29.39	0.8123	29.42	0.8758	34.92	0.9519	32.42	0.8780
RWKV-IR (Ours)	×3	DF2K	34.88	0.9308	30.77	0.8507	29.40	0.8124	29.43	0.8757	34.95	0.9520	32.43	0.8782
HAN [40]	×3	ReSyn	34.49	0.9278	30.36	0.8427	29.20	0.8110	28.73	0.8711	34.40	0.9500	32.38	0.8772
SwinIR [32]	×3	ReSyn	34.68	0.9296	30.71	0.8487	29.30	0.8113	29.20	0.8723	34.44	0.9505	32.41	0.8776
SRformer [67]	×3	ReSyn	34.48	0.9298	30.72	0.8488	29.34	0.8127	29.46	0.8771	34.53	0.9512	32.47	0.8786
MambaIR [21]	×3	ReSyn	34.74	0.9298	30.74	0.8492	29.35	0.8122	29.42	0.8766	34.53	0.9511	32.49	0.8803
RWKV-IR (Ours)	×3	ReSyn	34.77	0.9299	30.73	0.8491	29.34	0.8123	29.45	0.8768	34.55	0.9513	32.50	0.8805
HAN [40]	×4	DF2K	32.51	0.9001	28.85	0.7856	27.75	0.7440	26.88	0.8155	31.72	0.9015	30.60	0.8321
SwinIR [32]	×4	DF2K	32.74	0.9020	29.02	0.7920	27.83	0.7457	27.12	0.8162	31.75	0.9223	30.67	0.8335
SRFormer [67]	×4	DF2K	32.68	0.9010	29.03	0.7917	27.82	0.7458	27.38	0.8218	31.86	0.9234	30.72	0.8346
MambaIR [21]	×4	DF2K	32.73	0.9015	29.05	0.7923	27.87	0.7465	27.20	0.8176	31.83	0.9228	30.73	0.8345
RWKV-IR (Ours)	×4	DF2K	32.74	0.9016	29.04	0.7924	27.86	0.7466	27.21	0.8177	31.87	0.9233	30.74	0.8350
HAN [40]	×4	ReSyn	32.29	0.8991	28.59	0.7878	27.64	0.7420	26.58	0.8155	31.55	0.9201	30.67	0.8321
SwinIR [32]	×4	ReSyn	32.63	0.9009	28.98	0.7908	27.81	0.7449	27.16	0.8158	31.60	0.9220	30.75	0.8342
SRFormer [67]	×4	ReSyn	32.61	0.9007	28.98	0.7909	27.82	0.7452	27.42	0.8220	31.72	0.9225	30.79	0.8350
MambaIR [21]	×4	ReSyn	32.65	0.9009	29.00	0.7910	27.85	0.7458	27.21	0.8181	31.79	0.9224	30.81	0.8350
RWKV-IR (Ours)	×4	ReSyn	32.66	0.9011	29.02	0.7911	27.86	0.7459	27.24	0.8183	31.81	0.9226	30.83	0.8351



Figure 6. Illustration of Cross-Bi-WKV, which consists of two cross scanning Bi-WKV modules.

pixels are much smaller than that between the up and down neighboring pixels, and after applying the negative sign and exponential calculation, this leads to more attention to the horizontal direction than the vertical direction. Therefore, we propose a Cross-Bi-directional WKV module, which combines a horizontal direction Bi-WKV and a vertical direction Bi-WKV to achieve a balanced attention to horizontal and vertical pixels. The two Bi-WKV modules use different scanning orders when flattening the pixels into a 1D

sequence, one using the horizontal scanning order, and the other using the vertical scanning order, as shown in Fig. 6. And we use the average output of the two Bi-WKV modules to form the final output feature. After the DC-Shift, our Cross-Bi-directional attention mechanism with a linear complexity is formulated as follows and outputs a global attention result $wkv \in \mathbb{R}^{T \times C}$: $wkv = C\text{-Bi-WKV}(K, V) = Bi\text{-WKV}_{horizontal}(K_h, V_h) + Bi\text{-WKV}_{vertical}(K_v, V_v)$. The result wkv is then multiplied with $\sigma(R)$ to obtain the output O_s probability: $O_s = (\sigma(R_s) \odot wkv)W_O$. As the RWKV model continues to iterate and update, we believe that subsequent versions will bring greater improvements.

5. Experiments

Few previous methods have focused on the impact of training criteria on the performance comparison of restoration models. Many approaches [21, 32, 67] have instead opted to extend training time continuously to improve model per-

formance. This can lead to unfair comparisons in subsequent evaluations. Therefore, we construct a comprehensive training benchmark from two perspectives: measuring the model’s convergence ability and its restoration capability. In this section, we present the experimental benchmark and the training details of our proposed linear-complexity attention-based image restoration model. We then conduct a benchmark study comparing our method with other models. *Due to space limitations, only the results of classical SR tasks are shown in the main paper.* Please refer to the **Appendix** for the experiments of other IR tasks (light-weight SR, image denoising, JPEG artifacts reduction). Source codes are provided in the supplementary material.

5.1. Experimental Settings

Experimental Benchmark. We propose a unified training benchmark for different kinds of image restoration tasks. 1) *Super Resolution:* The commonly conducted SR tasks are lightweight SR and classical SR. For all compared methods, we set the same batch size and the same number of iterations for training. To show models’ convergence and restoration abilities, we compared different models in two number levels of training iterations. The batch size for lightweight SR model training is 64, and the training iterations are 50K and 500K. The batch size for classical SR model training is 32, and the training iterations are 100K and 500K. 2) *Image Denoising:* For Gaussian color denoising and gray-scale denoising tasks, the training batch size and the training iterations are set to 16 and 100K (500k for long training), respectively. 3) *JPEG Compression Artifact Reduction:* the batch size and training iterations are set to 16 and 100K (500k for high number level), respectively. *For more details about the model settings, please refer to the Appendix.*

Training Details. We conduct super-resolution (SR) training experiments on three datasets: DIV2K [44], DF2K [33], and our ReSyn. For lightweight SR, models are trained separately on the DIV2K and ReSyn datasets. For classic SR, models are trained separately on the DF2K and ReSyn datasets. In the training of image denoising models, we compare performance on the DFWB RGB dataset (a combined dataset of DIV2K [46], Flickr2K [33], BSD500 [2], and WED [37]) and our ReSyn dataset. During training, we crop the compressed images into 64×64 patches for image SR. We do not use pre-trained weights from the $\times 2$ model to initialize those of $\times 3$ and $\times 4$ but train the $\times 3$ and $\times 4$ models from scratch. For the denoising task, we crop the original images into 128×128 patches. We employ the Adam optimizer for training our RWKV-IR with $\beta_1 = 0.9$ and $\beta_2 = 0.999$. The initial learning rate is set at 2×10^{-4} and is decreased during training using the multi-step scheduler. Our models are trained with 8 NVIDIA V100 GPUs. Except for the batch size and training iterations for the compared methods, all other settings remain consistent with their

official codes.

5.2. Comparison on Image Super-Resolution

Classic Image Super-Resolution. Table 1 presents quantitative comparisons between RWKV-IR and state-of-the-art methods (HAN [40], SwinIR [32], SRFormer [67], and MambaIR [21]) on 100K training iters, which can show the convergence capability of models. Our method achieves optimal results on almost all five datasets for all scale factors. As shown, our RWKV-based baseline outperforms SwinIR by 0.08dB on Urban100 for x4 scale and MambaIR by 0.03dB, demonstrating the image restoration capability and quick convergence ability of our RWKV-IR. Furthermore, training our newly constructed ReSyn dataset also achieves decent performance, despite the overall quality of the data sources not being high. This also proves the feasibility of the image complexity-based dataset construction method. *The comparisons on long training iterations and other IR tasks could be found in the Appendix.*

5.3. Ablation Study

In this section, we conduct ablation studies to explore the effects of different designs of the core GLLB on the test dataset Urban100. These experiments can demonstrate the issues that need to be considered when applying the linear attention mechanism RWKV to image restoration models. They also provide an intuitive reflection of the problems mentioned earlier, offering insights for subsequent application research. To reduce training costs, all the models are lightweight models trained on the DIV2K dataset. The ablation studies results in Tab. 2, 3, 4 and 5 indicate that: (1) The original Q-Shift from the RWKV hinders the performance of the model on the image restoration task, since its simple feature substitution does not capture local similarity. (2) We propose the Depth-wise Convolution Shift (DC-Shift) to replace the Q-shift, which models relationships in local receptive fields, helping to enhance the restoration capabilities, thereby obtaining a PSNR improvement of 0.87dB. (3) Since the Bi-WKV pays unbalance attention to horizontal and vertical directions, our Cross Bi-WKV module that combines two Bi-WKV modules with different scanning orders further improves the performance of the image restoration model, with a PSNR improvement of 0.75dB. (4) The MLP module is not suitable for image restoration, a Channel Attention Block (CAB) or Channel Mix process can further improve the model performance. These experiments show the Cross-Bi-WKV module and the Depth-wise Conv Shift can help improve the performance. With the continuous iteration and upgrades of RWKV, we believe that subsequent versions of RWKV will bring genuine global attention, significantly enhancing the IR capabilities.

DC-Shift Position	Before SM	Between SM and CM	Behind CM	Parallel	Replace QS
PSNR \uparrow	32.41	32.54	32.51	32.65	32.95

Table 2. Ablation study of the insert position of Conv. SM, CM, and TS individually present Spatial Mix, Channel Mix, and Q shift.

WKV Setting	Bi-WKV	Cross-Bi-WKV
PSNR \uparrow	32.20	32.95

Table 3. The study of the different settings of WKV scanning methods. Ours settings of are in **Bold**

Shift Method	Q-Shift (p=1)	Q-Shift (p=0, w.o. shift)	DC-Shift (ks=3)	DC-Shift (ks=5)
PSNR \uparrow	32.08	32.69	32.95	32.84

Table 4. Ablation study of Shift settings (p in Q-Shift is the distance from neighboring pixels to the center; ks in DC-Shift is the kernel size).

FFN	MLP	CAB	Channel Mix
PSNR \uparrow	32.32	32.67	32.95

Table 5. The study of FFN modules (CAB means Channel Attention Block). Ours settings of are in **Bold**. The best scores are in **red**.

6. Conclusion

In this paper, we review the task of image restoration. We utilize the Gray Level Co-occurrence Matrix to construct an image complexity metric, which demonstrates the bias between complexity distributions of classic training datasets and test datasets. Based on this metric, we construct ReSyn, a new image restoration dataset that includes both real and generated images with balanced complexity. Additionally, we develop a novel benchmark for comparing image restoration models, focusing on two aspects: the convergence speed and the restoration capability. Moreover, from the perspective of linear attention mechanisms, we propose a novel RWKV-IR model, which integrates the RWKV into image restoration models, constructing a linear attention-based image restoration model. This inspires further exploration and enhancement of the effective receptive field of the model. Extensive experiments demonstrate the effectiveness of our proposed benchmark and RWKV-IR model.

References

- [1] Namhyuk Ahn, Byungkon Kang, and Kyung-Ah Sohn. Fast, accurate, and lightweight super-resolution with cascading residual network. In *Proceedings of the European conference on computer vision (ECCV)*, pages 252–268, 2018. **15**
- [2] Pablo Arbelaez, Michael Maire, Charles Fowlkes, and Jitendra Malik. Contour detection and hierarchical image segmentation. *IEEE transactions on pattern analysis and machine intelligence*, 33(5):898–916, 2010. **3, 8**
- [3] Marco Bevilacqua, Aline Roumy, Christine Guillemot, and Marie Line Alberi-Morel. Low-complexity single-image super-resolution based on nonnegative neighbor embedding. 2012. **3**
- [4] Nicolas Carion, Francisco Massa, Gabriel Synnaeve, Nicolas Usunier, Alexander Kirillov, and Sergey Zagoruyko. End-to-end object detection with transformers. In *European conference on computer vision*, pages 213–229. Springer, 2020. **3**
- [5] Lukas Cavigelli, Pascal Hager, and Luca Benini. Cas-cnn: A deep convolutional neural network for image compression artifact suppression. In *2017 International Joint Conference on Neural Networks (IJCNN)*, pages 752–759. IEEE, 2017. **3**
- [6] Hanting Chen, Yunhe Wang, Tianyu Guo, Chang Xu, Yiping Deng, Zhenhua Liu, Siwei Ma, Chunjing Xu, Chao Xu, and Wen Gao. Pre-trained image processing transformer. In *Proceedings of the IEEE/CVF conference on computer vision and pattern recognition*, pages 12299–12310, 2021. **1, 3**
- [7] Xiangyu Chen, Xintao Wang, Jiantao Zhou, Yu Qiao, and Chao Dong. Activating more pixels in image super-resolution transformer. In *Proceedings of the IEEE/CVF Conference on Computer Vision and Pattern Recognition*, pages 22367–22377, 2023. **1, 3, 4, 5, 6**
- [8] Xuhai Chen, Jiangning Zhang, Chao Xu, Yabiao Wang, Chengjie Wang, and Yong Liu. Better” cmos” produces clearer images: Learning space-variant blur estimation for blind image super-resolution. In *Proceedings of the IEEE/CVF conference on computer vision and pattern recognition*, pages 1651–1661, 2023. **3**
- [9] Zheng Chen, Yulun Zhang, Jinjin Gu, Linghe Kong, and Xiaokang Yang. Recursive generalization transformer for image super-resolution. *arXiv preprint arXiv:2303.06373*, 2023. **3**
- [10] Zheng Chen, Yulun Zhang, Jinjin Gu, Linghe Kong, Xiaokang Yang, and Fisher Yu. Dual aggregation transformer for image super-resolution. In *Proceedings of the IEEE/CVF international conference on computer vision*, pages 12312–12321, 2023. **1, 3**
- [11] Tao Dai, Jianrui Cai, Yongbing Zhang, Shu-Tao Xia, and Lei Zhang. Second-order attention network for single image super-resolution. In *Proceedings of the IEEE/CVF conference on computer vision and pattern recognition*, pages 11065–11074, 2019. **1, 3, 15**
- [12] Jia Deng, Wei Dong, Richard Socher, Li-Jia Li, Kai Li, and Li Fei-Fei. Imagenet: A large-scale hierarchical image database. In *2009 IEEE conference on computer vision and pattern recognition*, pages 248–255. Ieee, 2009. **3, 4, 13**
- [13] Chao Dong, Chen Change Loy, Kaiming He, and Xiaoou Tang. Learning a deep convolutional network for image super-resolution. In *Computer Vision—ECCV 2014: 13th European Conference, Zurich, Switzerland, September 6–12, 2014, Proceedings, Part IV 13*, pages 184–199. Springer, 2014. **1, 3**
- [14] Chao Dong, Yubin Deng, Chen Change Loy, and Xiaoou Tang. Compression artifacts reduction by a deep convolutional network. In *Proceedings of the IEEE international conference on computer vision*, pages 576–584, 2015. **3**
- [15] Alexey Dosovitskiy, Lucas Beyer, Alexander Kolesnikov, Dirk Weissenborn, Xiaohua Zhai, Thomas Unterthiner, Mostafa Dehghani, Matthias Minderer, Georg Heigold, Syl-

- vain Gelly, et al. An image is worth 16x16 words: Transformers for image recognition at scale. *arXiv preprint arXiv:2010.11929*, 2020. **3**
- [16] Yuchen Duan, Weiyun Wang, Zhe Chen, Xizhou Zhu, Lewei Lu, Tong Lu, Yu Qiao, Hongsheng Li, Jifeng Dai, and Wenhai Wang. Vision-rwkv: Efficient and scalable visual perception with rwkv-like architectures. *arXiv preprint arXiv:2403.02308*, 2024. **3**
- [17] Zhengcong Fei, Mingyuan Fan, Changqian Yu, Debang Li, and Junshi Huang. Diffusion-rwkv: Scaling rwkv-like architectures for diffusion models. *arXiv preprint arXiv:2404.04478*, 2024. **3**
- [18] Xueyang Fu, Zheng-Jun Zha, Feng Wu, Xinghao Ding, and John Paisley. Jpeg artifacts reduction via deep convolutional sparse coding. In *Proceedings of the IEEE/CVF International Conference on Computer Vision*, pages 2501–2510, 2019. **3**
- [19] Albert Gu and Tri Dao. Mamba: Linear-time sequence modeling with selective state spaces. *arXiv preprint arXiv:2312.00752*, 2023. **3**
- [20] Tiancheng Gu, Kaicheng Yang, Xiang An, Ziyong Feng, Dongnan Liu, Weidong Cai, and Jiankang Deng. Rwkv-clip: A robust vision-language representation learner. *arXiv preprint arXiv:2406.06973*, 2024. **3**
- [21] Hang Guo, Jinmin Li, Tao Dai, Zhihao Ouyang, Xudong Ren, and Shu-Tao Xia. Mambair: A simple baseline for image restoration with state-space model. *arXiv preprint arXiv:2402.15648*, 2024. **3, 5, 7, 8, 13, 14, 15, 16**
- [22] Qingdong He, Jiangning Zhang, Jinlong Peng, Haoyang He, Yabiao Wang, and Chengjie Wang. Pointrwkv: Efficient rwkv-like model for hierarchical point cloud learning. *arXiv preprint arXiv:2405.15214*, 2024. **3**
- [23] Jia-Bin Huang, Abhishek Singh, and Narendra Ahuja. Single image super-resolution from transformed self-exemplars. In *Proceedings of the IEEE conference on computer vision and pattern recognition*, pages 5197–5206, 2015. **3, 4**
- [24] Zheng Hui, Xinbo Gao, Yunchu Yang, and Xiumei Wang. Lightweight image super-resolution with information multi-distillation network. In *Proceedings of the 27th acm international conference on multimedia*, pages 2024–2032, 2019. **15**
- [25] Jiwon Kim, Jung Kwon Lee, and Kyoung Mu Lee. Accurate image super-resolution using very deep convolutional networks. In *Proceedings of the IEEE conference on computer vision and pattern recognition*, pages 1646–1654, 2016. **3**
- [26] Alexander Kirillov, Eric Mintun, Nikhila Ravi, Hanzi Mao, Chloe Rolland, Laura Gustafson, Tete Xiao, Spencer Whitehead, Alexander C Berg, Wan-Yen Lo, et al. Segment anything. In *Proceedings of the IEEE/CVF International Conference on Computer Vision*, pages 4015–4026, 2023. **4, 13**
- [27] Wei-Sheng Lai, Jia-Bin Huang, Narendra Ahuja, and Ming-Hsuan Yang. Deep laplacian pyramid networks for fast and accurate super-resolution. In *Proceedings of the IEEE conference on computer vision and pattern recognition*, pages 624–632, 2017. **3**
- [28] Wenbo Li, Kun Zhou, Lu Qi, Nianjuan Jiang, Jiangbo Lu, and Jiaya Jia. Lapar: Linearly-assembled pixel-adaptive regression network for single image super-resolution and beyond. *Advances in Neural Information Processing Systems*, 33:20343–20355, 2020. **15**
- [29] Wenbo Li, Xin Lu, Shengju Qian, Jiangbo Lu, Xiangyu Zhang, and Jiaya Jia. On efficient transformer-based image pre-training for low-level vision. *arXiv preprint arXiv:2112.10175*, 2021. **3**
- [30] Yawei Li, Yuchen Fan, Xiaoyu Xiang, Denis Demandolx, Rakesh Ranjan, Radu Timofte, and Luc Van Gool. Efficient and explicit modelling of image hierarchies for image restoration. In *Proceedings of the IEEE/CVF Conference on Computer Vision and Pattern Recognition*, pages 18278–18289, 2023. **1**
- [31] Yawei Li, Kai Zhang, Jingyun Liang, Jiezhang Cao, Ce Liu, Rui Gong, Yulun Zhang, Hao Tang, Yun Liu, Denis Demandolx, et al. Lsdir: A large scale dataset for image restoration. In *Proceedings of the IEEE/CVF Conference on Computer Vision and Pattern Recognition*, pages 1775–1787, 2023. **1, 3, 4**
- [32] Jingyun Liang, Jiezhang Cao, Guolei Sun, Kai Zhang, Luc Van Gool, and Radu Timofte. Swinir: Image restoration using swin transformer. In *Proceedings of the IEEE/CVF international conference on computer vision*, pages 1833–1844, 2021. **1, 3, 5, 7, 8, 13, 14, 15, 16**
- [33] Bee Lim, Sanghyun Son, Heewon Kim, Seungjun Nah, and Kyoung Mu Lee. Enhanced deep residual networks for single image super-resolution. In *Proceedings of the IEEE conference on computer vision and pattern recognition workshops*, pages 136–144, 2017. **1, 3, 4, 8, 15**
- [34] Tsung-Yi Lin, Michael Maire, Serge Belongie, James Hays, Pietro Perona, Deva Ramanan, Piotr Dollár, and C Lawrence Zitnick. Microsoft coco: Common objects in context. In *Computer Vision—ECCV 2014: 13th European Conference, Zurich, Switzerland, September 6–12, 2014, Proceedings, Part V 13*, pages 740–755. Springer, 2014. **4, 13**
- [35] Yue Liu, Yunjie Tian, Yuzhong Zhao, Hongtian Yu, Lingxi Xie, Yaowei Wang, Qixiang Ye, and Yunfan Liu. Vmamba: Visual state space model. *arXiv preprint arXiv:2401.10166*, 2024. **3**
- [36] Ze Liu, Yutong Lin, Yue Cao, Han Hu, Yixuan Wei, Zheng Zhang, Stephen Lin, and Baining Guo. Swin transformer: Hierarchical vision transformer using shifted windows. In *Proceedings of the IEEE/CVF international conference on computer vision*, pages 10012–10022, 2021. **3**
- [37] Kede Ma, Zhengfang Duanmu, Qingbo Wu, Zhou Wang, Hongwei Yong, Hongliang Li, and Lei Zhang. Waterloo exploration database: New challenges for image quality assessment models. *IEEE Transactions on Image Processing*, 26(2):1004–1016, 2016. **3, 8**
- [38] David Martin, Charless Fowlkes, Doron Tal, and Jitendra Malik. A database of human segmented natural images and its application to evaluating segmentation algorithms and measuring ecological statistics. In *Proceedings Eighth IEEE International Conference on Computer Vision. ICCV 2001*, pages 416–423. IEEE, 2001. **3**
- [39] Yusuke Matsui, Kota Ito, Yuji Aramaki, Azuma Fujimoto, Toru Ogawa, Toshihiko Yamasaki, and Kiyoharu Aizawa. Sketch-based manga retrieval using manga109 dataset. *Multimedia Tools and Applications*, 76:21811–21838, 2017. **3**

- [40] Ben Niu, Weilei Wen, Wenqi Ren, Xiangde Zhang, Lianping Yang, Shuzhen Wang, Kaihao Zhang, Xiaochun Cao, and Haifeng Shen. Single image super-resolution via a holistic attention network. In *Computer Vision–ECCV 2020: 16th European Conference, Glasgow, UK, August 23–28, 2020, Proceedings, Part XII 16*, pages 191–207. Springer, 2020. [7](#), [8](#), [15](#)
- [41] Bo Peng, Eric Alcaide, Quentin Anthony, Alon Albalak, Samuel Arcadinho, Stella Biderman, Huanqi Cao, Xin Cheng, Michael Chung, Matteo Grella, et al. Rwkv: Reinventing rrms for the transformer era. *arXiv preprint arXiv:2305.13048*, 2023. [2](#), [3](#), [5](#)
- [42] Bo Peng, Daniel Goldstein, Quentin Anthony, Alon Albalak, Eric Alcaide, Stella Biderman, Eugene Cheah, Teddy Ferdinan, Haowen Hou, Przemysław Kazienko, et al. Eagle and finch: Rwkv with matrix-valued states and dynamic recurrence. *arXiv preprint arXiv:2404.05892*, 2024. [3](#)
- [43] Zhen Qin, Xiaodong Han, Weixuan Sun, Bowen He, Dong Li, Dongxu Li, Yuchao Dai, Lingpeng Kong, and Yiran Zhong. Toeplitz neural network for sequence modeling. *arXiv preprint arXiv:2305.04749*, 2023. [3](#)
- [44] Radu Timofte, Eirikur Agustsson, Luc Van Gool, Ming-Hsuan Yang, and Lei Zhang. Ntire 2017 challenge on single image super-resolution: Methods and results. In *Proceedings of the IEEE conference on computer vision and pattern recognition workshops*, pages 114–125, 2017. [1](#), [3](#), [4](#), [8](#)
- [45] Ashish Vaswani, Noam Shazeer, Niki Parmar, Jakob Uszkoreit, Llion Jones, Aidan N Gomez, Łukasz Kaiser, and Illia Polosukhin. Attention is all you need. *Advances in neural information processing systems*, 30, 2017. [3](#)
- [46] Jue Wang, Wentao Zhu, Pichao Wang, Xiang Yu, Linda Liu, Mohamed Omar, and Raffay Hamid. Selective structured state-spaces for long-form video understanding. In *Proceedings of the IEEE/CVF Conference on Computer Vision and Pattern Recognition*, pages 6387–6397, 2023. [8](#)
- [47] Xintao Wang, Ke Yu, Shixiang Wu, Jinjin Gu, Yihao Liu, Chao Dong, Yu Qiao, and Chen Change Loy. Esrgan: Enhanced super-resolution generative adversarial networks. In *The European Conference on Computer Vision Workshops (ECCVW)*, 2018. [3](#)
- [48] Yunxuan Wei, Shuhang Gu, Yawei Li, Radu Timofte, Longcun Jin, and Hengjie Song. Unsupervised real-world image super resolution via domain-distance aware training. In *Proceedings of the IEEE/CVF Conference on Computer Vision and Pattern Recognition*, pages 13385–13394, 2021. [3](#)
- [49] Kun Yuan, Shaopeng Guo, Ziwei Liu, Aojun Zhou, Fengwei Yu, and Wei Wu. Incorporating convolution designs into visual transformers. In *Proceedings of the IEEE/CVF international conference on computer vision*, pages 579–588, 2021. [6](#)
- [50] Syed Waqas Zamir, Aditya Arora, Salman Khan, Munawar Hayat, Fahad Shahbaz Khan, and Ming-Hsuan Yang. Restormer: Efficient transformer for high-resolution image restoration. In *Proceedings of the IEEE/CVF conference on computer vision and pattern recognition*, pages 5728–5739, 2022. [3](#), [13](#), [16](#)
- [51] Roman Zeyde, Michael Elad, and Matan Protter. On single image scale-up using sparse-representations. In *Curves and Surfaces: 7th International Conference, Avignon, France, June 24-30, 2010, Revised Selected Papers 7*, pages 711–730. Springer, 2012. [3](#)
- [52] Shuangfei Zhai, Walter Talbott, Nitish Srivastava, Chen Huang, Hanlin Goh, Ruixiang Zhang, and Josh Susskind. An attention free transformer, 2021. [3](#)
- [53] Jiangning Zhang, Chao Xu, Jian Li, Wenzhou Chen, Yabiao Wang, Ying Tai, Shuo Chen, Chengjie Wang, Feiyue Huang, and Yong Liu. Analogous to evolutionary algorithm: Designing a unified sequence model. *Advances in Neural Information Processing Systems*, 34:26674–26688, 2021. [3](#)
- [54] Jiangning Zhang, Chao Xu, Jian Li, Yue Han, Yabiao Wang, Ying Tai, and Yong Liu. Scsnet: An efficient paradigm for learning simultaneously image colorization and super-resolution. In *Proceedings of the AAAI Conference on Artificial Intelligence*, pages 3271–3279, 2022. [3](#)
- [55] Jiangning Zhang, Xiangtai Li, Jian Li, Liang Liu, Zhucun Xue, Boshen Zhang, Zhengkai Jiang, Tianxin Huang, Yabiao Wang, and Chengjie Wang. Rethinking mobile block for efficient attention-based models. In *2023 IEEE/CVF International Conference on Computer Vision (ICCV)*, pages 1389–1400. IEEE Computer Society, 2023. [3](#)
- [56] Jiale Zhang, Yulun Zhang, Jinjin Gu, Yongbing Zhang, Linghe Kong, and Xin Yuan. Accurate image restoration with attention retractable transformer. In *ICLR*, 2023. [3](#)
- [57] Kai Zhang, Wangmeng Zuo, Yunjin Chen, Deyu Meng, and Lei Zhang. Beyond a gaussian denoiser: Residual learning of deep cnn for image denoising. *IEEE transactions on image processing*, 26(7):3142–3155, 2017. [1](#), [3](#), [13](#), [16](#)
- [58] Kai Zhang, Wangmeng Zuo, Shuhang Gu, and Lei Zhang. Learning deep cnn denoiser prior for image restoration. In *Proceedings of the IEEE conference on computer vision and pattern recognition*, pages 3929–3938, 2017. [13](#), [16](#)
- [59] Kai Zhang, Wangmeng Zuo, and Lei Zhang. Ffdnet: Toward a fast and flexible solution for cnn-based image denoising. *IEEE Transactions on Image Processing*, 27(9):4608–4622, 2018. [13](#), [16](#)
- [60] Kai Zhang, Yawei Li, Wangmeng Zuo, Lei Zhang, Luc Van Gool, and Radu Timofte. Plug-and-play image restoration with deep denoiser prior. *IEEE Transactions on Pattern Analysis and Machine Intelligence*, 44(10):6360–6376, 2021. [13](#), [16](#)
- [61] Kai Zhang, Yawei Li, Wangmeng Zuo, Lei Zhang, Luc Van Gool, and Radu Timofte. Plug-and-play image restoration with deep denoiser prior. *IEEE Transactions on Pattern Analysis and Machine Intelligence*, 44(10):6360–6376, 2021. [3](#)
- [62] Xindong Zhang, Hui Zeng, Shi Guo, and Lei Zhang. Efficient long-range attention network for image super-resolution. In *European Conference on Computer Vision*, pages 649–667. Springer, 2022. [15](#)
- [63] Yulun Zhang, Kunpeng Li, Kai Li, Lichen Wang, Bineng Zhong, and Yun Fu. Image super-resolution using very deep residual channel attention networks. In *Proceedings of the European conference on computer vision (ECCV)*, pages 286–301, 2018. [1](#)
- [64] Yulun Zhang, Kunpeng Li, Kai Li, Lichen Wang, Bineng Zhong, and Yun Fu. Image super-resolution using very deep

- residual channel attention networks. In *ECCV*, 2018. 3, 13, 16
- [65] Yulun Zhang, Yapeng Tian, Yu Kong, Bineng Zhong, and Yun Fu. Residual dense network for image super-resolution. In *Proceedings of the IEEE conference on computer vision and pattern recognition*, pages 2472–2481, 2018. 3
- [66] Yucheng Zhao, Guangting Wang, Chuanxin Tang, Chong Luo, Wenjun Zeng, and Zheng-Jun Zha. A battle of network structures: An empirical study of cnn, transformer, and mlp. *arXiv preprint arXiv:2108.13002*, 2021. 6
- [67] Yupeng Zhou, Zhen Li, Chun-Le Guo, Song Bai, Ming-Ming Cheng, and Qibin Hou. Srformer: Permuted self-attention for single image super-resolution. *arXiv preprint arXiv:2303.09735*, 2023. 1, 4, 7, 8, 13, 14, 15

Exploring Real&Synthetic Dataset and Linear Attention in Image Restoration

Supplementary Material

A1. More details of Our ReSyn Dataset

In this section, we further provide details on the construction of our ReSyn dataset. The process of final filtering based on our GLCM image complexity metric is shown in Fig. A1.

Our ReSyn dataset contains images from four sources, including ImageNet [12], COCO2017 [34], SAM [26], and MidJourney. For ImageNet, we first remove images with a resolution of less than 800×800 . Since the details in the images from ImageNet are not rich and relatively blurry, then the images of blurring and noise degradation are filtered. Finally, through image complexity filtering, we choose 1,200 images from the ImageNet. Half of the images have a complexity greater than zero.

For COCO2017 [34], almost all of the images are medium-resolution images, we follow the method of ImageNet filtering and include 1,200 images from COCO2017.

For SAM, most images have a resolution of over 2K. For privacy purposes, many of the images in the dataset containing faces and sensitive information are mosaiced. Therefore, we manually remove the images that include the mosaics, leaving only the clear images. After this step, we use the same filtering method as ImageNet and include 6,000 images from SAM.

For MidJourney, we first crawled more than 30,000 high-quality images from the web. And then after filtering, 3,600 images are left to form the dataset.

A2. Model details

In Tab. A1, we provide the model setting details for different image restoration tasks, which could serve as a reference for model construction. It should be noted that the number of embedding channels in RWKV-based models must be an integer that is a multiple of 16.

A3. More Image Restoration Experiments

In this section we supplement quantitative comparisons on other image restoration tasks, including 1) light-weight SR, 2) image denoising, and 3) JPEG artifacts reduction. These experiments show the generality of our model.

A3.1. Classical Image Super-Resolution

In Tab. A3, we compare RWKV-IR with other methods on 500K training iterations. Our newly proposed image restoration models also have a good performance once the training iteration is long. It also has a linear computational

complexity, which makes the model save the computational overhead and is more conducive to the scaling of the model.

A3.2. Lightweight Image Super-Resolution

We also provide comparison of our RWKV-IR-light with state-of-the-art lightweight image SR methods: SwinIR [32], SRFormer [67] and MambaIR [21]. Including PSNR and SSIM, we also compare the total number of parameters and MACs (multiply-accumulate operations) to show the model size and the computational complexity of different models. We compare the metrics gained from different training datasets used. The results on 50K training iterations are shown in Tab. A2 and on 500K are shown in Tab. A4. On the small number of training iterations, RWKV-IR outperforms MambaIR-light by 0.10dB on Urban100 with an x4 scale, with a similar parameter number and MACs when trained on the DIV2K dataset. Using ReSyn gets a similar result with DIV2K, since the lightweight models' training iteration is small, our ReSyn could also show a favorable performance. On the large number of training iterations, our proposed linear-complexity attention-based image restoration model also shows competitive performance. This indicates that our model not only converges quickly, but also has excellent image restoration capabilities.

A3.3. Gaussian Color Image Denoising

As shown in Tab. A5, we conduct the quantitative comparison between our RWKV-IR and the SOTA methods IRCNN [58], FFDNet [59], DnCNN [57], SwinIR [32], Restormer [50] and MambaIR [21] on long training iterations. All the models are trained on the DFWB-RGB dataset. Our method achieves competitive metrics on all four datasets.

A3.4. Grayscale Image Denoising

As shown in Tab. A6, we conduct the quantitative comparison between our RWKV-IR and the SOTA methods IRCNN [58], FFDNet [59], DnCNN [57], SwinIR [32] on grayscale image denoising task. All models are trained on long iterations of 500K and on DFWB-gray dataset. Our method achieves competitive metrics on all three datasets.

A3.5. JPEG Compression Artifact Reduction

Tab. A7 shows the comparison of RWKV-IR with state-of-the-art JPEG compression artifact reduction methods: ARCNN [64], DnCNN-3 [57], DRUNet [60] and SwinIR [32]. Following [32, 60], we test different methods on two benchmark datasets (Classic5 and LIVE1) for JPEG quality factors 10, 20, 30 and 40. It can be seen that the proposed RWKV-IR

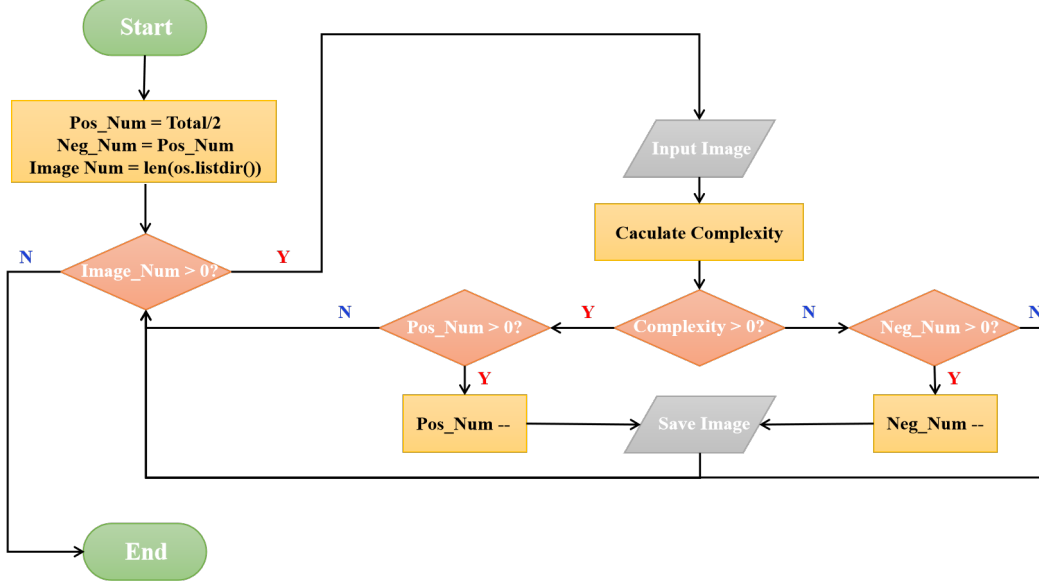


Figure A1. The final filtering procedure based on GLCM image complexity of the ReSyn dataset.

Table A1. The model setting details for different image restoration tasks.

	Classic SR	Light-Weight SR	Denoising	JPEG
Embed channel	192	48	192	192
Image size	64	64	128	128
Blocks setting	[6,6,6,6,6]	[6,6,6,6]	[6,6,6,6,6]	[6,6,6,6,6]
WKV setting	Cross WKV	Layer Cross WKV	Cross WKV	Cross WKV

Table A2. Quantitative comparison on lightweight image super-resolution with state-of-the-art methods on 50K training iterations. The best scores are in red.

Method	scale	#param	MACs	dataset	Set5		Set14		BSDS100		Urban100		Manga109		ReSyn	
					PSNR	SSIM	PSNR	SSIM	PSNR	SSIM	PSNR	SSIM	PSNR	SSIM	PSNR	SSIM
SwinIR-light [32]	×2	878K	195.6G	DIV2K	37.76	0.9598	33.34	0.9161	32.05	0.8981	31.55	0.9225	38.08	0.9759	34.81	0.9276
SRFormer-light [67]	×2	853K	236G	DIV2K	37.68	0.9593	33.29	0.915	32.03	0.8977	31.56	0.9224	38.11	0.9763	34.93	0.9279
MambaIR [21]	×2	859K	198.1G	DIV2K	37.88	0.9601	33.50	0.9168	32.13	0.8993	31.97	0.9268	38.50	0.9767	34.96	0.9288
RWKV-IR (Ours)	×2	863K	198.5G	DIV2K	37.98	0.9604	33.51	0.9167	32.13	0.8991	32.15	0.9283	38.66	0.9769	34.96	0.9287
SwinIR-light [32]	×2	878K	195.6G	ReSyn	37.62	0.9594	33.29	0.9155	32.04	0.8980	31.54	0.9224	37.87	0.9760	34.92	0.9280
SRFormer-light [67]	×2	853K	236G	ReSyn	37.62	0.9594	33.29	0.9155	32.04	0.8980	31.54	0.9224	37.87	0.9760	34.92	0.9280
MambaIR [21]	×2	859K	198.1G	ReSyn	37.68	0.9596	33.43	0.9162	32.10	0.8989	31.80	0.9251	38.52	0.9770	35.06	0.9290
RWKV-IR (Ours)	×2	863K	198.5G	ReSyn	37.79	0.9601	33.36	0.9165	32.09	0.8990	31.98	0.9263	38.65	0.9775	35.11	0.9295
SwinIR-light [32]	×3	886K	87.2G	DIV2K	34.11	0.9246	30.22	0.8399	28.97	0.8023	27.71	0.8426	33.00	0.9408	31.79	0.8687
SRFormer-light [67]	×3	861K	105G	DIV2K	34.24	0.9259	30.26	0.8408	29.01	0.8036	27.88	0.8474	33.21	0.9424	31.85	0.8699
MambaIR [21]	×3	867K	88.7G	DIV2K	34.32	0.9263	30.27	0.8406	29.05	0.8039	28.07	0.8506	33.39	0.9432	31.96	0.8711
RWKV-IR (Ours)	×3	873K	91.7G	DIV2K	34.35	0.9265	30.20	0.8411	29.07	0.8044	28.13	0.8516	33.57	0.9439	31.95	0.8705
SwinIR-light [32]	×3	886K	87.2G	ReSyn	34.07	0.9251	30.14	0.8385	28.96	0.8020	27.72	0.8427	32.87	0.9409	31.86	0.8692
SRFormer-light [67]	×3	861K	105G	ReSyn	34.15	0.9255	30.19	0.8386	28.99	0.8021	27.82	0.8445	33.07	0.9418	31.91	0.8695
MambaIR [21]	×3	867K	88.7G	ReSyn	34.20	0.9260	30.21	0.8391	29.04	0.8037	28.04	0.8490	33.29	0.9430	32.03	0.8713
RWKV-IR (Ours)	×3	873K	91.7G	ReSyn	34.29	0.9264	30.14	0.8392	29.06	0.8038	28.15	0.8505	33.46	0.9439	32.05	0.8713
SwinIR-light [32]	×4	897K	49.6G	DIV2K	31.97	0.8913	28.47	0.7786	27.48	0.7336	25.76	0.7753	30.06	0.9031	30.11	0.8225
SRFormer-light [67]	×4	873K	62.8G	DIV2K	32.00	0.8915	28.46	0.7784	27.48	0.7337	25.84	0.7780	30.12	0.9039	30.11	0.8228
MambaIR [21]	×4	879K	50.6G	DIV2K	32.12	0.8935	28.51	0.7796	27.51	0.7339	25.94	0.7804	30.27	0.9051	30.22	0.8241
RWKV-IR (Ours)	×4	887K	51.6G	DIV2K	32.14	0.8942	28.46	0.7809	27.57	0.7365	26.07	0.7848	30.48	0.9074	30.24	0.8246
SwinIR-light [32]	×4	897K	49.6G	ReSyn	31.93	0.8914	28.42	0.7778	27.45	0.7320	25.74	0.7742	30.04	0.9031	30.14	0.8222
SRFormer-light [67]	×4	873K	62.8G	ReSyn	31.97	0.8920	28.49	0.7782	27.47	0.7323	25.85	0.7771	30.16	0.9047	30.18	0.8230
MambaIR [21]	×4	879K	50.6G	ReSyn	32.09	0.8938	28.53	0.7793	27.52	0.7337	26.02	0.7824	30.36	0.9070	30.31	0.8252
RWKV-IR (Ours)	×4	887K	51.6G	ReSyn	32.16	0.8941	28.45	0.7806	27.56	0.7351	26.13	0.7850	30.47	0.9084	30.34	0.8251

Table A3. Quantitative comparison on **classic image super-resolution** with state-of-the-art methods on 500K training iterations.

Method	scale	Set5		Set14		BSDS100		Urban100		Manga109	
		PSNR	SSIM	PSNR	SSIM	PSNR	SSIM	PSNR	SSIM	PSNR	SSIM
EDSR [33]	×2	38.11	0.9602	33.92	0.9195	32.32	0.9013	32.93	0.9351	39.10	0.9773
SAN [11]	×2	38.31	0.9620	34.07	0.9213	32.42	0.9028	33.10	0.9370	39.32	0.9792
HAN [40]	×2	38.27	0.9614	34.16	0.9217	32.41	0.9027	33.35	0.9385	39.46	0.9785
ELAN [62]	×2	38.36	0.9620	34.20	0.9228	32.45	0.9030	33.44	0.9391	39.62	0.9793
SwinIR [32]	×2	38.42	0.9623	34.46	0.9250	32.53	0.9041	33.81	0.9427	39.92	0.9797
SRFormer [67]	×2	38.51	0.9627	34.44	0.9253	32.57	0.9046	34.09	0.9449	40.07	0.9802
MambaIR [21]	×2	38.60	0.9628	34.69	0.9260	32.60	0.9048	34.17	0.9443	40.33	0.9806
RWKV-IR (Ours)	×2	38.62	0.9629	34.63	0.9254	32.58	0.9045	34.20	0.9446	40.34	0.9804
EDSR [33]	×3	34.65	0.9280	30.52	0.8462	29.25	0.8093	28.80	0.8653	34.17	0.9476
SAN [11]	×3	34.75	0.9300	30.59	0.8476	29.33	0.8112	28.93	0.8671	34.30	0.9494
HAN [40]	×3	34.75	0.9299	30.67	0.8483	29.32	0.8110	29.10	0.8705	34.48	0.9500
ELAN [62]	×3	34.90	0.9313	30.80	0.8504	29.38	0.8124	29.32	0.8745	34.73	0.9517
SwinIR [32]	×3	34.97	0.9318	30.93	0.8534	29.46	0.8145	29.75	0.8826	35.12	0.9537
SRformer [67]	×3	35.02	0.9323	30.94	0.8540	29.48	0.8156	30.04	0.8865	35.26	0.9543
MambaIR [21]	×3	35.13	0.9326	31.06	0.8541	29.53	0.8162	29.98	0.8838	35.55	0.9549
RWKV-IR (Ours)	×3	35.16	0.9328	31.02	0.8538	29.52	0.8159	30.02	0.8839	35.57	0.9548
EDSR [33]	×4	32.46	0.8968	28.80	0.7876	27.71	0.7420	26.64	0.8033	31.02	0.9148
SAN [11]	×4	32.64	0.9003	28.92	0.7888	27.78	0.7436	26.79	0.8068	31.18	0.9169
HAN [40]	×4	32.64	0.9002	28.90	0.7890	27.80	0.7442	26.85	0.8094	31.42	0.9177
ELAN [62]	×4	32.75	0.9022	28.96	0.7914	27.83	0.7459	27.13	0.8167	31.68	0.9226
SwinIR [32]	×4	32.92	0.9044	29.09	0.7950	27.92	0.7489	27.45	0.8254	32.03	0.9260
SRFormer [67]	×4	32.93	0.9041	29.08	0.7953	27.94	0.7502	27.68	0.8311	32.21	0.9271
MambaIR [21]	×4	33.13	0.9054	29.25	0.7971	28.01	0.7510	27.80	0.8303	32.48	0.9281
RWKV-IR (Ours)	×4	33.14	0.9056	29.20	0.7968	27.99	0.7511	27.83	0.8305	32.51	0.9285

Table A4. Quantitative comparison on **lightweight image super-resolution** with state-of-the-art methods on 500K training iterations.

Method	scale	#param	MACs	Set5		Set14		BSDS100		Urban100		Manga109	
				PSNR	SSIM	PSNR	SSIM	PSNR	SSIM	PSNR	SSIM	PSNR	SSIM
CARN [1]	×2	1,592K	222.8G	37.76	0.9590	33.52	0.9166	32.09	0.8978	31.92	0.9256	38.36	0.9765
IMDN [24]	×2	694K	158.8G	38.00	0.9605	33.63	0.9177	32.19	0.8996	32.17	0.9283	38.88	0.9774
LAPAR-A [28]	×2	548K	171.0G	38.01	0.9605	33.62	0.9183	32.19	0.8999	32.10	0.9283	38.67	0.9772
SwinIR-light [32]	×2	878K	195.6G	38.14	0.9611	33.86	0.9206	32.31	0.9012	32.76	0.9340	39.12	0.9783
SRFormer-light [67]	×2	853K	236G	38.23	0.9613	33.94	0.9209	32.36	0.9019	32.91	0.9353	39.28	0.9785
MambaIR [21]	×2	859K	198.1G	38.16	0.9610	34.00	0.9212	32.34	0.9017	32.92	0.9356	39.31	0.9779
RWKV-IR (Ours)	×2	859K	198.1G	38.22	0.9614	33.98	0.9210	32.37	0.9018	32.95	0.9359	39.34	0.9781
CARN [1]	×3	1,592K	118.8G	34.29	0.9255	30.29	0.8407	29.06	0.8034	28.06	0.8493	33.50	0.9440
IMDN [24]	×3	703K	71.5G	34.36	0.9270	30.32	0.8417	29.09	0.8046	28.17	0.8519	33.61	0.9445
LAPAR-A [28]	×3	544K	114.0G	34.36	0.9267	30.34	0.8421	29.11	0.8054	28.15	0.8523	33.51	0.9441
SwinIR-light [32]	×3	886K	87.2G	34.62	0.9289	30.54	0.8463	29.20	0.8082	28.66	0.8624	33.98	0.9478
SRFormer-light [67]	×3	861K	105G	34.67	0.9296	30.57	0.8469	29.26	0.8099	28.81	0.8655	34.19	0.9489
MambaIR [21]	×3	867K	88.7G	34.72	0.9296	30.63	0.8475	29.29	0.8099	29.00	0.8689	34.39	0.9495
RWKV-IR (Ours)	×3	867K	88.7G	34.76	0.9301	30.59	0.8471	29.32	0.8096	29.04	0.8693	34.37	0.9491
CARN [1]	×4	1,592K	90.9G	32.13	0.8937	28.60	0.7806	27.58	0.7349	26.07	0.7837	30.47	0.9084
IMDN [24]	×4	715K	40.9G	32.21	0.8948	28.58	0.7811	27.56	0.7353	26.04	0.7838	30.45	0.9075
LAPAR-A [28]	×4	659K	94.0G	32.15	0.8944	28.61	0.7818	27.61	0.7366	26.14	0.7871	30.42	0.9074
SwinIR-light [32]	×4	897K	49.6G	32.44	0.8976	28.77	0.7858	27.69	0.7406	26.47	0.7980	30.92	0.9151
SRFormer-light [67]	×4	873K	62.8G	32.51	0.8988	28.82	0.7872	27.73	0.7422	26.67	0.8032	31.17	0.9165
MambaIR [21]	×4	879K	50.6G	32.51	0.8993	28.85	0.7876	27.75	0.7423	26.75	0.8051	31.26	0.9175
RWKV-IR (Ours)	×4	879K	50.6G	32.53	0.8995	28.82	0.7875	27.78	0.7426	26.79	0.8052	31.28	0.9179

Table A5. Quantitative comparison on **gaussian color image denoising** with state-of-the-art methods.

Method	BSD68			Kodak24			McMaster			Urban100		
	$\sigma=15$	$\sigma=25$	$\sigma=50$	$\sigma=15$	$\sigma=25$	$\sigma=50$	$\sigma=15$	$\sigma=25$	$\sigma=50$	$\sigma=15$	$\sigma=25$	$\sigma=50$
IRCNN [58]	33.86	31.16	27.86	34.69	32.18	28.93	34.58	32.18	28.91	33.78	31.20	27.70
FFDNet [59]	33.87	31.21	27.96	34.63	32.13	28.98	34.66	32.35	29.18	33.83	31.40	28.05
DnCNN [57]	33.90	31.24	27.95	34.60	32.14	28.95	33.45	31.52	28.62	32.98	30.81	27.59
DRUNet [60]	34.30	31.69	28.51	35.31	32.89	29.86	35.40	33.14	30.08	34.81	32.60	29.61
SwinIR [32]	34.42	31.78	28.56	35.34	32.89	29.79	35.61	33.20	30.22	35.13	32.90	29.82
Restormer [50]	34.40	31.79	28.60	35.47	33.04	30.01	35.61	33.34	30.30	35.13	32.96	30.02
MambaIR [21]	34.44	31.82	28.64	35.35	32.92	29.87	35.63	33.36	30.32	35.17	32.99	30.06
RWKV-IR (Ours)	34.43	31.79	28.62	35.37	32.98	29.92	35.62	33.35	30.33	35.19	33.02	30.10

Table A6. Quantitative comparison on **grayscale image denoising** with state-of-the-art methods.

Method	Set12			BSD68			Urban100		
	$\sigma=15$	$\sigma=25$	$\sigma=50$	$\sigma=15$	$\sigma=25$	$\sigma=50$	$\sigma=15$	$\sigma=25$	$\sigma=50$
IRCNN [58]	32.76	30.37	27.12	31.63	29.15	26.19	32.46	29.80	26.22
FFDNet [59]	32.75	30.43	27.32	31.63	29.19	26.29	32.40	29.90	26.50
DnCNN [57]	33.86	30.44	27.18	31.73	29.23	26.23	32.64	29.95	26.26
DRUNet [60]	33.25	30.94	27.90	31.91	29.48	26.59	33.44	31.11	27.96
SwinIR [32]	33.36	31.01	27.91	31.97	29.50	26.58	33.70	31.30	27.98
MambaIR [21]	34.44	31.82	28.64	35.35	32.92	29.87	35.63	33.36	30.32
RWKV-IR (Ours)	34.46	31.85	28.66	35.33	32.90	29.84	35.64	33.35	30.34

Table A7. Quantitative comparison on **JPEG compression artifact reduction** with state-of-the-art methods. We show scores of average PSNR/SSIM/PSNR-B.

Method	Classic5				LIVE1			
	$q=10$	$q=20$	$q=30$	$q=40$	$q=10$	$q=20$	$q=30$	$q=40$
ARCNN [64]	29.03/0.7929/28.76	31.15/0.8517/30.59	32.51/0.8806/31.98	33.32/0.8953/32.79	28.96/0.8076/28.77	31.29/0.8733/30.79	32.67/0.9043/32.22	33.63/0.9198/33.14
DnCNN-3 [57]	29.40/0.8026/29.13	31.63/0.8610/31.19	31.63/0.8610/31.19	33.77/0.9003/33.20	29.19/0.8123/28.90	31.59/0.8802/31.07	32.98/0.9090/32.34	33.96/0.9247/33.28
DRUNet [60]	30.16/0.8234/29.81	32.39/0.8734/31.80	33.59/0.8949/32.82	34.41/0.9075/33.51	29.79/0.8278/29.48	32.17/0.8899/31.69	33.59/0.9166/32.99	34.58/0.9312/33.93
SwinIR [32]	30.27/0.8249/29.95	32.52/0.8748/31.99	33.73/0.8961/33.03	34.52/0.9082/33.66	29.86/0.8287/29.50	32.25/0.8909/31.70	33.69/0.9174/33.01	34.67/0.9317/33.88
RWKV-IR (Ours)	30.35/0.8261/30.04	32.63/0.8760/32.05	33.81/0.8972/33.12	34.61/0.9091/33.71	29.94/0.8296/29.62	32.34/0.8915/31.81	33.78/0.9185/33.12	34.78/0.9323/33.95

has average PSNR gains of at least 0.07dB and 0.08dB on two testing datasets for different quality factors.